

## Research Article

# Seismic Performance of Exterior Steel Ring-Stiffener Joint

Zhaoqiang Zhang <sup>1,2</sup>, Yanru Sa <sup>1</sup>, Yong Yao <sup>1</sup> and Junhai Zhao <sup>2</sup>

<sup>1</sup>*School of Civil Engineering and Architecture, Southwest University of Science and Technology, Mianyang 621010, Sichuan, China*

<sup>2</sup>*School of Civil Engineering, Chang'an University, Xi'an 710061, Shaanxi, China*

Correspondence should be addressed to Yanru Sa; [sayanru@163.com](mailto:sayanru@163.com)

Received 21 March 2019; Revised 25 May 2019; Accepted 17 September 2019; Published 7 November 2019

Academic Editor: Chun-Qing Li

Copyright © 2019 Zhaoqiang Zhang et al. This is an open access article distributed under the Creative Commons Attribution License, which permits unrestricted use, distribution, and reproduction in any medium, provided the original work is properly cited.

We study the seismic performance of the exterior steel ring-stiffener (ESRS) joint, a member that is used to connect a steel beam to a square steel tubular column filled with steel fibre recycled concrete for seismic resistance. To this end, the influence of seismic factors such as axial compression ratio and beam-column linear stiffness ratio on seven specimens is studied. A physical test is conducted on the specimens with a series of cyclic loadings. The testing and analysis of hysteretic loops and skeleton curves of the ESRS joints revealed the seismic performance characteristics including failure mode, rigidity, ductility, bearing-capacity degradation, and energy dissipation capacity. The results reveal (a) damage to the specimens at the beam-end near the joint, (b) no failure at the joints' core area and column, (c) appearance of a plastic hinge at the beam-end near the joint, and (d) plump spindle-shaped hysteretic loops and normal rigidity degradation curves in the specimens. The specimens are then simulated with the finite element method (FEM) and the results are compared with those of the physical test.

## 1. Introduction

Recycled coarse aggregates (RCA) from waste concrete can be extracted by crushing and cleaning concrete debris. Recycled concrete, which is a new type of green building material, is produced by substituting a percentage of its natural coarse aggregates (NCA) with RCA. By this method, waste concrete can be reutilised as a resource, and NCA can be conserved. In regular concrete-filled steel tubes (CFST), the exterior steel tube confines the concrete and the concrete in return supports the steel tube. Thus, CFST improves the strength, plasticity, and ductility of concrete inside external steel tubes, avoid or delay local buckling of the exterior steel tube, and increase its stability. Therefore, the material properties of both concrete and steel tube can be integrated and utilised [1]. The recycled-concrete-filled steel-tube column inherits the advantages of high bearing capacity, good seismic performance, and convenient construction of CFST columns. The literature [2–12] reveals that the performance of CFST can be improved by adding steel fibres to the concrete, and that this technical method could have

broad applications in high-rise buildings and large-span structures. Research also shows that the recycled-concrete-filled steel tubes can meet the performance of an ordinary steel tube under most conditions. In addition, Li et al. [2] numerically analysed the axial compressive properties of a steel tubular short column filled with steel-fibre high-strength concrete. Yin [3] studied the axial compressive properties of steel-fibre-lightweight-aggregate-concrete-filled steel tubular column by exposing it to flames. Gopal and Manoharan [4] conducted an experimental study on the eccentrically compressed, fibre-reinforced-concrete-filled slender circular steel tubes.

In this study, a new type of ESRS joint, which connects an H-shaped beam linked to a concrete slab to a square steel fibre recycled concrete (SFRC)-filled steel tubular column for improved earthquake resistance, is proposed. The study considers the advantages of the square CFST, SFRC, and ESRS joints, and the influence of slabs on the joints. Seven specimens are fabricated and tested, to study the seismic performance of ESRS. Through a physical test and finite element method (FEM) simulation, the seismic indices of the

ESRS joints—failure mechanism, deformability, bearing capacity, and energy dissipation capacity—are analysed. We believe this study will help lay the foundations of a sound theoretical system and promote the development, recycling, and reusing of waste concrete and SFRC in engineering practice.

## 2. Experimental Program

**2.1. Specimen Design.** Seven ESRS joint specimens were designed and fabricated based on the axial compressive ratios, beam-column linear stiffness ratios, numbers of bolts located in the joints' core area, and types of slab (including the recycled concrete slab and composite slab linked to the profiled steel sheet). Among them, specimen SJD-4 had four M10 high-strength bolts of class 10.9, which are located in the joint's core area. Specimens SJD-1~SJD-6 had a slab that is connected to its beam, while specimen SJD-7 did not. The axial compressive ratio can be validated through the adjusted load of a vertically set hydraulic jack. By adjusting the cross section of steel beams, the beam-column linear stiffness ratio can be controlled. The parameters of the specimens are presented in Table 1. Some specimens are shown in Figure 1.

**2.2. Material Properties.** The steel tubes are made of Q235 grade steel. Table 2 shows mechanical parameters of the steel used for the specimens, in accordance with the literature [13].

The proportions of SFRC per cubic metric are 584 kg of cement, 499 kg of sand, 855 kg of RCA, 368 kg of NCA, and 233 kg of water. The substitutive rate of the RCA is 70%. The dimensions of the curved steel fibres are  $0.7\text{ mm} \times 0.7\text{ mm} \times 35\text{ mm}$ . The steel fibre content is 1%, taken from the author's previous research [14, 15]. The numerical value of the standard compressive cubic strength for concrete,  $f_{cu,k}$ , is  $42.6\text{ N/mm}^2$ .

**2.3. Test Setup.** As shown in Figure 2, the vertical hydraulic jack with a bearing capacity of 1,000 kN is installed at the top of the column. A ball hinge is installed at the bottom of the column. The left end of the beam is free to move, and it was connected to a 250 kN hydraulic actuator that is linked to the beam of the reaction frame. The hydraulic actuator applies a cyclic load to the left beam-end of a specimen. To avoid instability and offset of the column during the loading, a lateral support is connected to the upper-end of the column.

The bearing capacity of each concrete-filled steel tubular column can be calculated per the literature [16–18]. The constant vertical load, which depends on the axial compressive ratio, was applied on the top of the column by a hydraulic jack with bearing capacity of 1,000 kN.

Figure 3 shows the cyclic loading test adopted for this study. The tests were performed by displacing the specimen. The reversal of cyclic loads was symmetric [19]. One cyclic loading was applied on the specimen at displacement <math>\leq 15\text{ mm}</math>. At displacement  $\geq 15\text{ mm}$ , three cyclic loadings were applied. At displacement  $\leq 30\text{ mm}$ , the displacement increment was 3 mm. At displacement  $> 30\text{ mm}$ , the

increment was 6 mm. The test was terminated when the applied load was less than 85% of the peak load.

Before each testing, the cells and sensors were checked to ensure that they were working well. Then, a preload was applied vertically to eliminate the initial imperfections of the test setup and allow the specimen to properly contact the testing device. After the checking and validation of the cells and sensors, a design vertical load was applied in two or three steps, and held for 2 min. Following that, a cyclic force was applied according to the loading procedure.

## 3. Test Phenomenon and Failure Mode

The specific failure phenomena are shown in Figure 4. The failure phenomena of specimens are listed in Table 3. The failure characteristics of specimens, obtained via observation and analysis of the failure, are summarised as follows:

- (1) In the elastic, elastic-plastic, and failure stages, a plastic hinge formed gradually at the beam-end near the joint. With tiny displacements and strains, the column and the joint were elastic. Therefore, the designed joint specimens meet the seismic principles of strong column and weak beam and strong joint and weak member.
- (2) In the testing phase, ESRS and the joints between them and the column were left undeformed. As the ESRS joint can effectively transmit and distribute the load, the distribution of stresses within the joint's core area was more uniform. This contributes to the seismic performance of joints.
- (3) Due to the composite effect of the slabs, both the joint's rigidity and the steel beam's stability were enhanced.

## 4. Experimental Results

**4.1. Hysteretic Curves.** The hysteretic curves are comprehensive reflections of the responses of structures or members subjected to cyclic loads, and are of great significance to the analysis of their seismic behaviour [20]. The hysteretic force vs. displacement curves of beam-end far from the joints are shown in Figure 5. The following conclusions are drawn from Figure 5:

- (1) Specimens develop plump, spindle-shaped hysteretic curves, and show improved energy dissipation capacity and displacement ductility.
- (2) When the displacement is smaller, the specimens are in the elastic stage, develop almost linear hysteretic loops with smaller envelopes, and have smaller residual deformations and energy dissipation capacities. As the displacement increases, the specimens move into the elastic-plastic stage. With the increasing displacement, the specimens gain curved hysteretic loops, which move gradually toward the displacement axis, with larger envelop areas, larger energy dissipation capacities, and greater rigidity

TABLE 1: Parameters of the specimens.

Specimen	Column dimension $D \times t \times L$	Steel beam sectional dimension $H \times B \times t_w \times t_f$	Axial compressive ratio, $n$	Slab type	Specimen type
SJD-1	150 × 3 × 1,500	150 × 75 × 5 × 5.5	0.07	Reinforced recycled concrete slab	Common joint
SJD-2	150 × 3 × 1,500	150 × 75 × 5 × 5.5	0.18	Reinforced recycled concrete slab	Common joint
SJD-3	150 × 3 × 1,500	150 × 75 × 5 × 5.5	0.29	Reinforced recycled concrete slab	Common joint
SJD-4	150 × 3 × 1,500	150 × 75 × 5 × 5.5	0.18	Reinforced recycled concrete slab	Joint with bolts
SJD-5	150 × 3 × 1,500	200 × 100 × 5.5 × 6	0.18	Reinforced recycled concrete slab	Common joint
SJD-6	150 × 3 × 1,500	150 × 75 × 5 × 5.5	0.18	Slab composited with profiled steel sheet	Common joint
SJD-7	150 × 3 × 1,500	150 × 75 × 5 × 5.5	0.18	—	Common joint

degeneration. With the increasing displacement, cracks begin to appear around the plates and columns. After the specimens have yielded, the loading cycles are applied three times for each displacement. When the three hysteretic loops at a given displacement are compared, the last two loops are smaller than the first loop and the envelop areas of the last two loops decrease. This demonstrates strength degradation, decline of energy dissipation capacity, and damage accumulation in the specimens.

- (3) Due to the composite effects of slabs, the specimens have a larger rigidity and bearing capacity in the negative direction than in the positive one.

**4.2. Skeleton Curves.** A skeleton curve can be obtained by connecting every peak load of the given displacements. The characteristic points can be obtained from a skeleton curve, such as yield displacement and load, peak displacement and load, and ultimate displacement and load. From the skeleton curve, mechanical properties such as ductility, energy dissipation, strength degradation, and rigidity degradation can be obtained.

The skeleton curves obtained from the tests are shown in Figure 6. They reflect the respective influences of axial compressive ratios, beam-column linear stiffness ratio, high-strength bolts, slab types, slab, etc.

- (1) The elastic rigidity increases with increasing axial compressive ratio. The skeleton curves and bearing capacities of different specimens are close to each other.
- (2) Specimens SJD-5 and SJD-2 have the same axial compressive ratio, but the beam-column linear stiffness ratio of specimen SJD-5 is higher. The peak load of SJD-5 is 58% higher than SJD-2 in the positive direction, and 42.7% higher in the negative direction. It follows that the rigidity and bearing capacity of specimens increase with an increasing beam-column linear stiffness ratio.

- (3) Specimens SJD-4 and SJD-2 have the same axial compressive ratio, but SJD-4 has high-strength bolts in its joint's core area. The skeleton curves of specimens SJD-4 and SJD-2 are close with each other. It follows that the high-strength bolts in the joint's core area hardly have any influence on the rigidity and bearing capacity.
- (4) Specimen SJD-2 has a reinforced recycled concrete slab connected to its beam, while SJD-6 has a slab composited with a profiled steel sheet. The peak load of SJD-2 is 35.9% higher than that of SJD-6 in the positive direction, and 9.9% higher than that of SJD-6 in the negative direction. Compared with the specimen with a slab-profiled-steel-sheet composite, the specimen with a recycled reinforced concrete slab has a larger rigidity and bearing capacity.
- (5) Specimen SJD-2 has a slab, while SJD-7 does not. The peak load of SJD-2 is 30.3% higher than that of SJD-7 in the positive direction, and 57.4% higher than that of SJD-7 in the negative direction. Compared with the specimen without a slab, the specimen with a slab has a larger rigidity and bearing capacity.

**4.3. Rigidity Degeneration.** Effective rigidity is one of the most important indicators of seismic performance of structures and members. The effective rigidity is presented in terms of the loop rigidity [20, 21]:

$$K_j = \frac{\sum_{i=1}^n P_{ij}}{\sum_{i=1}^n u_{ij}}, \quad (1)$$

where  $P_{ij}$  represents the peak load of the  $i$ -th loading cycle at the  $j$ -th displacement of  $\Delta_j$ ,  $u_{ij}$  refers to the peak displacement of the  $i$ -th loading cycle at the  $j$ -th displacement of  $\Delta_j$ , and  $n$  is the number of loading cycles.

At the initial loading stage, the rigidity of specimens decreases drastically. At the final loading stage, as the concrete cracks have fully propagated, and the specimens move into the plastic stage, the rigidity drops slowly. Thus, as shown in Figure 7, following the cracking of concrete and

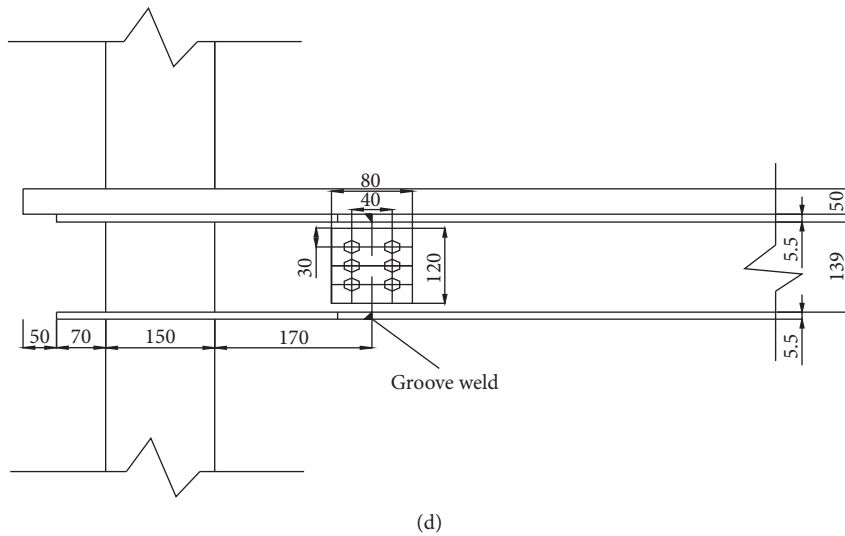
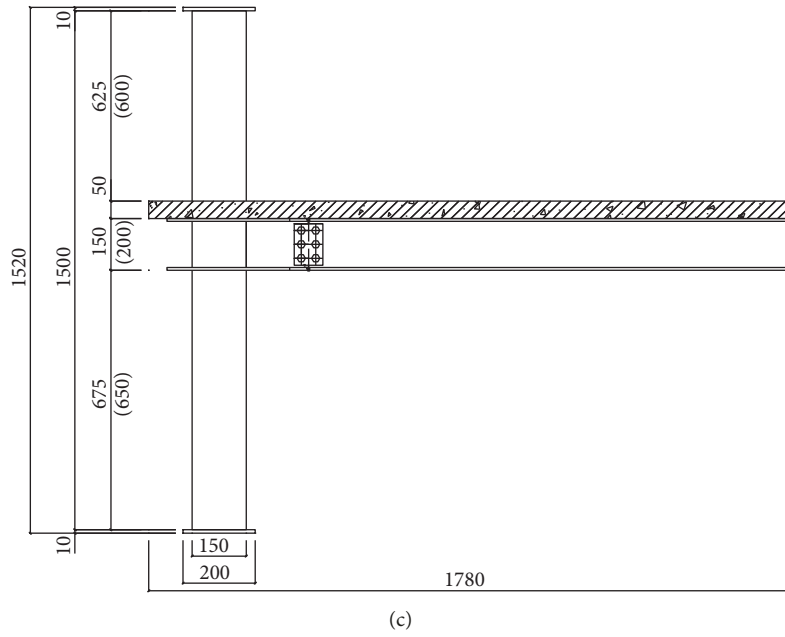
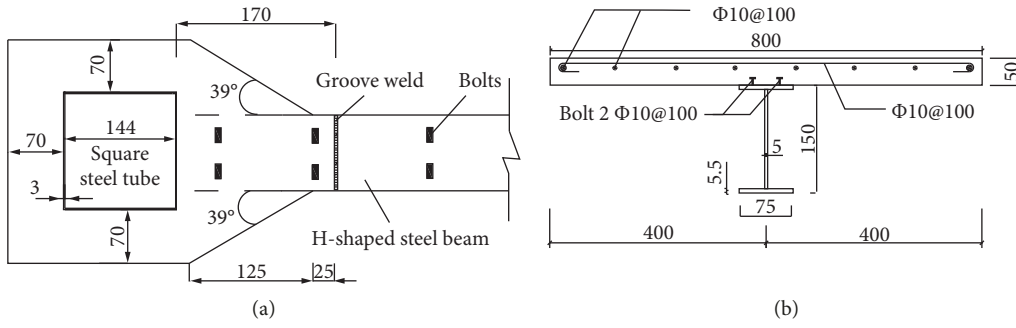


FIGURE 1: Continued.

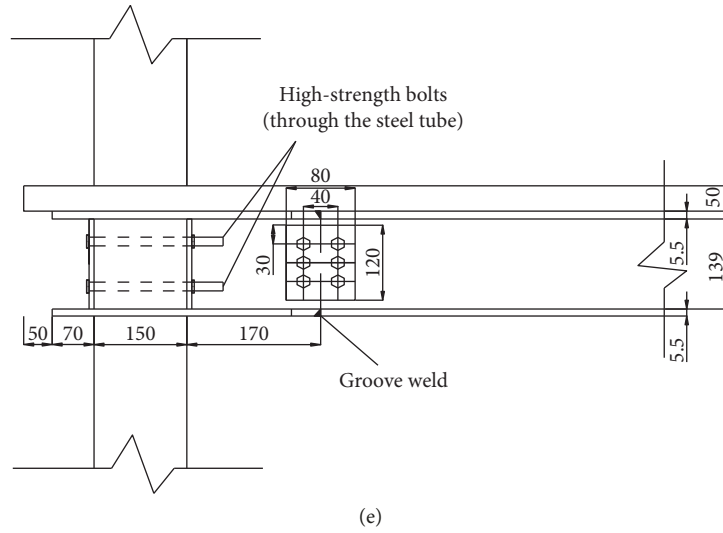


FIGURE 1: Illustrative drawing of joints. (a) Exterior steel ring-stiffener (all dimensions in mm). (b) Cross section of beam-slab system (all dimensions in mm). (c) Common joint with a concrete slab (all dimensions in mm). (d) Common joint (all dimensions in mm). (e) Joint with bolts (all dimensions in mm).

TABLE 2: Mechanical properties of various steels for the specimens.

Specimen	Thickness or diameter (mm)	Yield strength (MPa)	Tensile strength (MPa)	Elastic modulus (GPa)
Steel tubular column	3.0	347	400	196
Stiffening plate	5.0	337	475	211
Flange of the steel beam	5.5	295	461	206
	6.0	270	438	200
Web-plate of the steel beam	5.0	281	448	190
	5.5	283	448	190
Reinforcing bar	Φ10	389	543	209

damage accumulation of steel, the rigidity decreases with the increasing absolute displacement. Furthermore, the initial rigidity increases with the increasing beam-column linear stiffness ratio.

For the specimen with a slab connected to its steel beam, the rigidities in both the directions are different at various loading stages. In the initial loading stage, the slab and steel beam are tightly combined, and the initial rigidity in the negative direction is larger than that in the positive direction. In the final loading stage, with the cracks fully extended in the concrete slab, the concrete slab is damaged, the composite effects between the slab and the steel beam disappear, and the final rigidities in both the directions are close to each other.

**4.4. Ductility.** The ductility of a structure or a member defines its capability to endure plastic deformation, with a relative higher load applied. Ductility is an important parameter representing the deformation capability of a structure or a member, and it is of great significance for the evaluation of seismic performance of structures [22, 23]. Ductility is usually expressed by the ductility coefficient. According to the different definitions of deformation, there are three ductility coefficients of structures and members: curvature ductility coefficient, corner ductility

coefficient, and displacement ductility coefficient. Among them, the curvature ductility coefficient only indicates the characteristics of a certain section, while the corner ductility coefficient and the displacement ductility coefficient can reflect the ductility of the structure and the member more macroscopically. Ductility is usually expressed by a ductility index ( $\mu$ ). In general, the larger the value of  $\mu$ , the better the ductility of the joint. Equation (2) is given for calculating the ductility index. In the formula, displacements  $\Delta_u$  and  $\Delta_y$  of the beam-end far from the joint are used to calculate the ductility index, and can be determined according to the method described in the literature [20].

$$\mu = \frac{\Delta_u}{\Delta_y}, \quad (2)$$

where  $\Delta_u$  represents the displacement corresponding to the peak load  $P_u$ , and  $\Delta_y$  is the displacement corresponding to the yield load  $P_y$ .

Table 4 shows the yield load, the yield displacement, the peak load, the peak displacement, and the ductility indices of the specimens. The following is a summary of the results from Table 4:

- (1) The average value of the ductility indices of the specimens is 2.10.

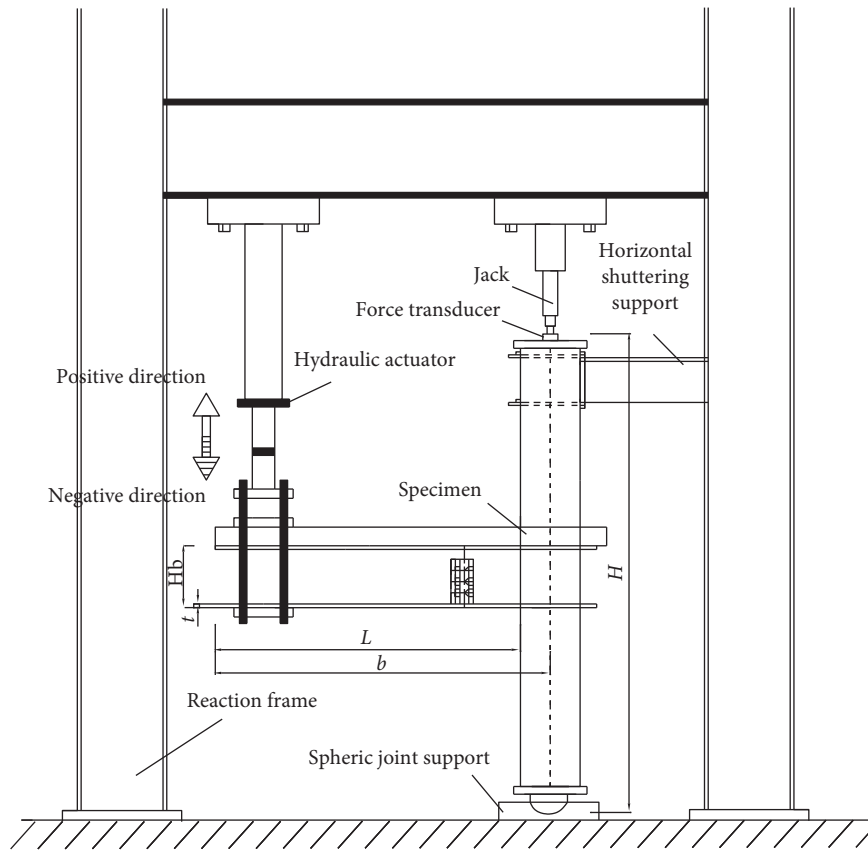


FIGURE 2: Test setup.

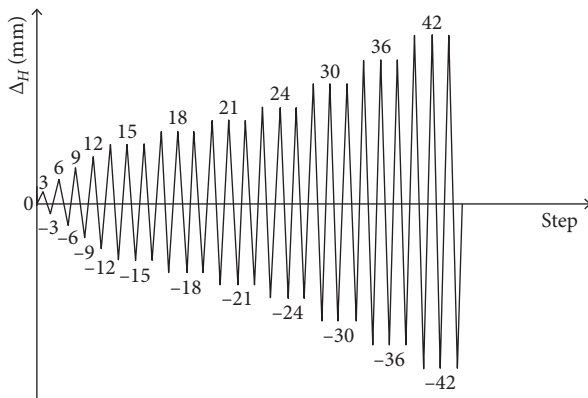


FIGURE 3: Loading procedure adopted for cyclic tests.

(2) The compressive capacity of concrete is significantly higher than its tensile capacity; so, it is reasonable to assume that the concrete can carry only the compressive stress and neglect its tensile capacity in engineering practice. When loading in the positive direction, the beam-end far from the joint moves downward, the concrete slab carries a negligible tensile stress, and the top flange of the steel beam carries nearly the whole tensile force. When loading in the negative direction, the beam-end far from the joint moves upward, a compressive stress is exerted on the concrete slab, and the concrete slab can work

in tandem with the top flange of the steel beam to carry the compressive force. The differences in the mechanical properties of the composite beam-slab system can induce significant differences in the bearing capacity and ductility index in both the directions. For example, specimen SJD-6 has a slab connected to its steel beam, and its yield load and peak load in negative direction are 2.3 and 1.7 times those in the positive direction, respectively. Furthermore, its ductility index in the positive direction is 1.8 times that in the negative direction. This is because, in the negative loading, the recycled reinforced concrete slab is compressed and the plate joints with the top flange of the steel beam in resisting the pressure and deformation. In the positive loading, the recycled reinforced concrete slab has poor tensile strength and cracks easily, so that the section size of the plate is reduced, and the tension is basically assumed by the top flange of the steel beam.

(3) A comparison of the ductility indices of specimens with the same axial compressive ratio revealed that the indices of SJD-4, SJD-5, and SJD-6 were relatively lower than those of SJD-2. This indicates that such structural fabrications could have negative effects on the ductility of specimens, as high-strength bolts settled in the joint's core area increased the beam-column linear stiffness ratio and



FIGURE 4: Failure phenomena of specimens. (a) Cracks appear at corners of the column. (b) Local buckling occurs at the bottom flange of the steel beam. (c) Rupture of weld seam occurs at the bottom flange of the steel beam. (d) Cracks parallel to the longer side of the slab. (e) Rupture of weld seam occurs at the top flange of the steel beam.

the recycled concrete slab composited with a profiled steel sheet.

- (4) The axial compression ratio has little effect on the bearing capacity of the specimen. This is because the specimen is broken in the plastic hinge area of the beam and the column is in the elastic stage.

**4.5. Energy Dissipation.** The energy dissipation capacity is another important index for studying the seismic performance of structures and members. In a loading-unloading hysteretic loop, the energy absorbed by the loading process is generally larger than the energy discharged by the unloading process. The difference between the energy

TABLE 3: Failure phenomena of specimens.

Specimen	Failure phenomena
SJD-1	(a), (b), (c), (d)
SJD-2	(a), (c), (d)
SJD-3	(a), (c), (d)
SJD-4	(a), (b), (c), (d)
SJD-5	(a), (b), (c), (d)
SJD-6	(b), (c), (d)
SJD-7	(e)

absorbed and energy discharged is energy dissipation, which is represented by the area enclosed by a hysteretic loop. The plumper the loop and the larger its enclosed area, the larger the energy dissipation capacity. In engineering practice, the energy dissipation coefficient,  $E$ , and the effective viscous damping factor,  $h_e$ , are generally used to evaluate the energy dissipation capacity of structures and members [24, 25]. The equivalent damping coefficient ( $h_e$ ) was defined by formulas (3) and (4). As shown in Figure 8,  $S_{BEF}$  and  $S_{DEF}$  are areas under the BEF and DEF curves, respectively, and  $S_{AOB}$  and  $S_{COD}$  are the triangular areas of AOB and COD, respectively.

$$h_e = \frac{E}{2\pi}, \quad (3)$$

$$E = \frac{S_{EBF} + S_{FDE}}{S_{AOBA} + S_{ODC}}. \quad (4)$$

Table 5 shows the  $E$  and  $h_e$  obtained. The relationship between  $h_e$  and the loading cycle is shown in Figure 9. As shown in the table, the numerical values of  $h_e$  are in the range of 0.161–0.198 at a displacement of 36 mm, and their average value is 0.180. The effective viscous damping factors obtained from the tests are almost twice those of the reinforced concrete joints. It follows that the joints studied have better energy dissipation capacity, and hence can meet the requirements of structural seismic design.

With larger effective viscous damping factors, the seismic dissipation capacity of specimens with a slab is better than those without a slab. The axial compressive ratio has negative effects on seismic dissipation capacity, and the effective viscous factor decreases with increasing axial compressive ratio.

A comparison of SJD-4 and SJD-2 reveals that their effective viscous factors are close to each other. From this, the high-strength bolts in the joint's core area have no influence on the seismic dissipation capacity. As shown in Figure 9, the effective viscous factors increase with displacement—the larger the displacement, the greater the energy dissipation. At a given displacement, the energy dissipation capacity decreases with increasing loading cycle. The plastic hinge developing at the beam-end near the joint could improve the energy dissipation capacity of specimens.

## 5. Finite Element Analysis of Specimens

**5.1. Establishment of Finite Element Model.** The C3D8R element and structural meshing method were used to mesh

the steel and recycled concrete. A meshed specimen is shown in Figure 10.

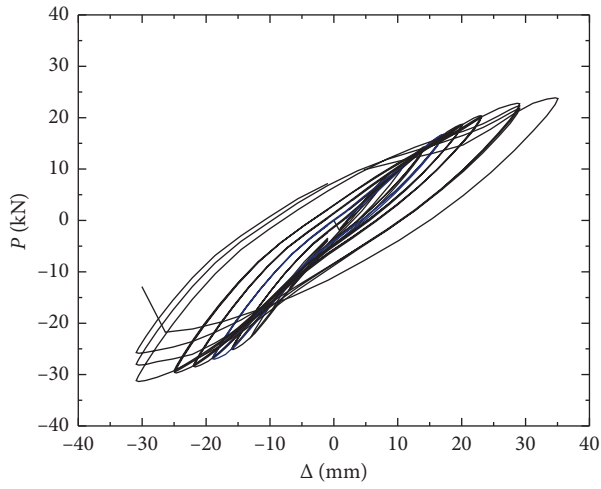
The loading and boundary conditions of the specimen are shown in Figure 11. The displacement constraints in the  $x$  and  $z$  directions, and the rotational constraints in the  $y$  and  $z$  directions are enforced on the top of the column. The displacement constraints in the  $x$ ,  $y$ , and  $z$  directions, and the rotational constraints in the  $y$  and  $z$  directions are applied at the bottom of the column. The column can only move in the vertical direction and rotate in the  $y$ - $o$ - $z$  plane. The displacement constraint in the  $x$  direction is enforced at the reference point of the beam, so that the beam can move only in the  $y$ - $o$ - $z$  plane. Two steps were adopted for the loading: (a) Exertion of a vertical force on the top of the column, and (b) application of cyclic load on the left beam-end.

**5.2. Material Constitutive Relationship.** The double-straight-lines-strengthened model is used as a constitutive relationship of steel. In the case of the constitutive relationship of recycled concrete used in the slab, the model developed by Xiao [24] is used as the compressive constitutive relationship, and the tensile model of ordinary concrete is used as the tensile constitutive relationship [25]. In the case of the constitutive relationship of SFRC used in the column, the model presented by Yang [26] and Meng [27] is used as the compressive constitutive relationship, and the tensile constitutive relationship is the same with the concrete used in the slab. There are few references for the constitutive relationship of steel fibre recycled concrete in the literature. Upon the addition of steel fibre, the strength gain of the specimen is not obvious and the column is basically in the elastic state during the whole stress cycle. In addition, the method for determining the damage coefficient of concrete proposed by Birtel and Mark [28] is adopted.

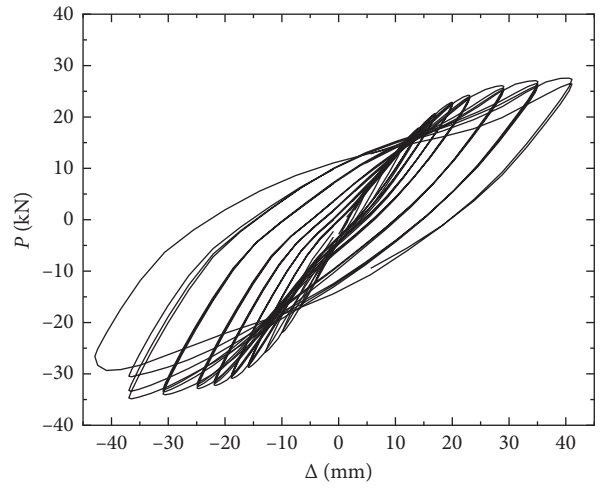
**5.3. Contact Pairs Settings.** For the contact between the steel tube and the concrete, the tangential force is considered along with the Coulomb friction criterion, and the normal force along with the “hard contact.” A nonlinear spring unit is generally used to simulate the contact between the top flange of the steel beam and the concrete, as there are studs connecting the top flange of the steel beam to the concrete slab. The embedded connection is used to simulate the contact between the reinforcing bars and the concrete slab. In this case, the reinforcing bars and the concrete slab need to be modelled separately (see Figure 12).

### 5.4. Comparison between FEM and Physical Test Results

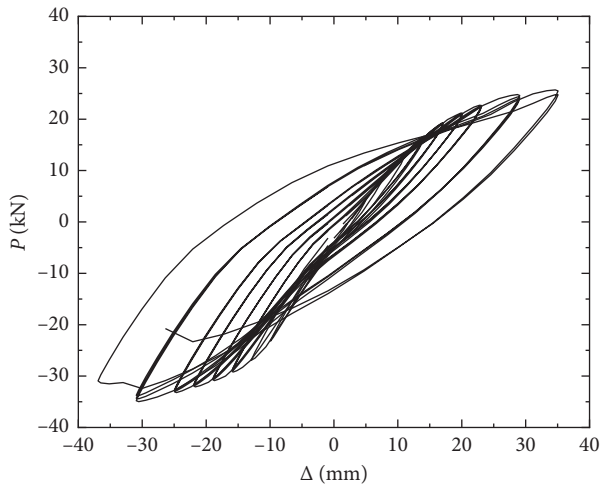
**5.4.1. Hysteretic Curves.** Figure 13 illustrates the experimental and simulated hysteretic curves for the joints studied. The hysteretic curves obtained from the tests and the FEM simulation are in good agreement with each other. The error margin between the simulated and experimental curves is less than 10%. We also found that the specimens have spindle-shaped hysteretic curves. These curves imply that the ESRs joint specimens have better ductility and seismic



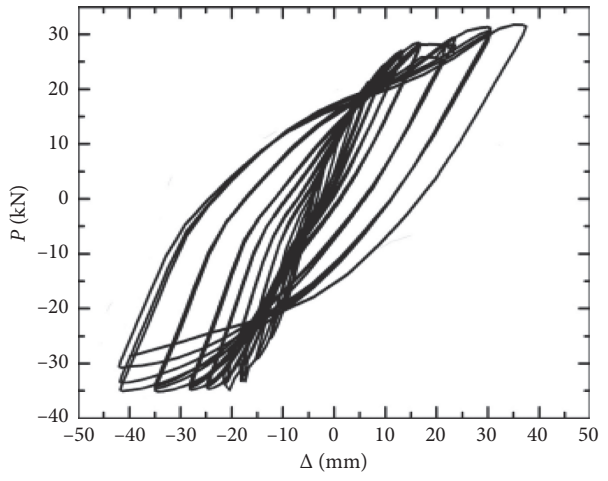
(a)



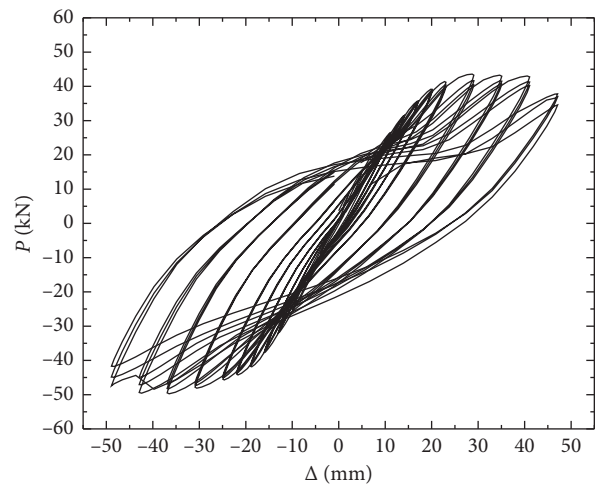
(b)



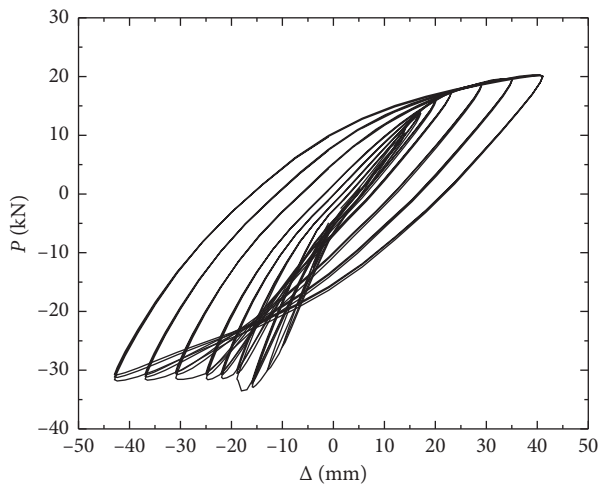
(c)



(d)

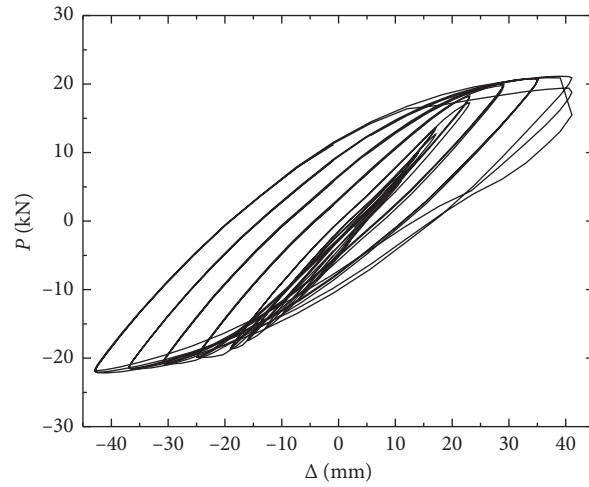


(e)



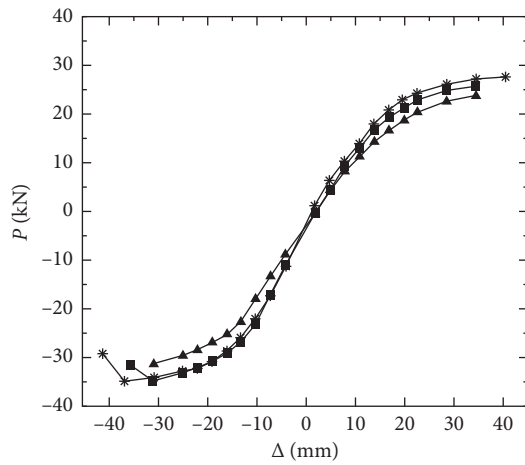
(f)

FIGURE 5: Continued.



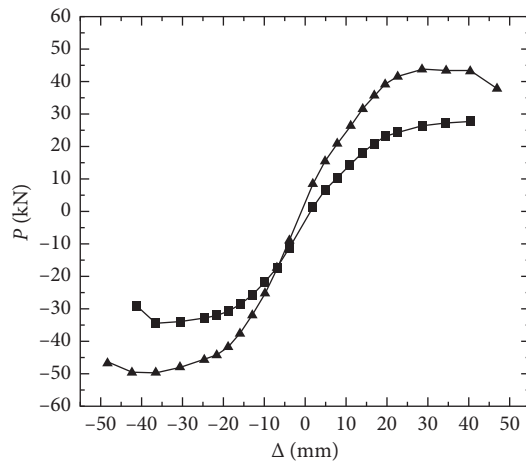
(g)

FIGURE 5: Hysteretic curves of the specimens. (a) SJD-1. (b) SJD-2. (c) SJD-3. (d) SJD-4. (e) SJD-5. (f) SJD-6. (g) SJD-7.



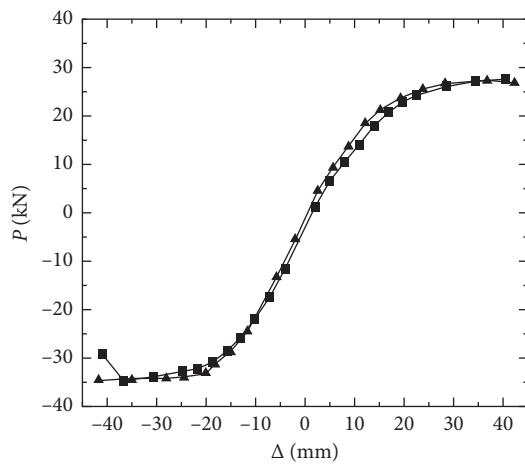
▲ SJD-1  
\* SJD-2  
■ SJD-3

(a)



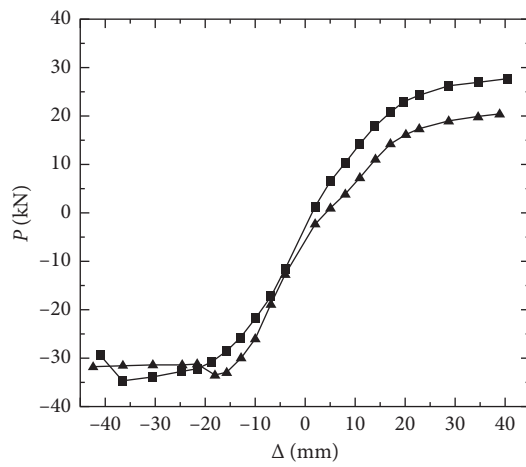
■ SJD-2  
▲ SJD-5

(b)



■ SJD-2  
▲ SJD-4

(c)



■ SJD-2  
▲ SJD-6

(d)

FIGURE 6: Continued.

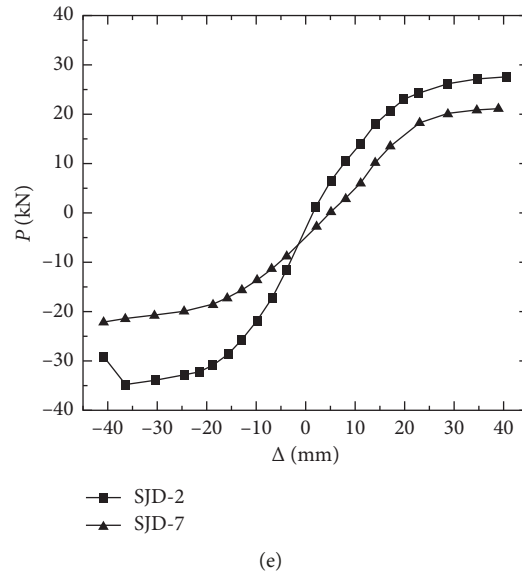


FIGURE 6: Skeleton curves. (a) Influence of axial compressive ratio. (b) Influence of linear stiffness ratio. (c) Influence of high-strength bolts. (d) Influence of the slab type. (e) Influence of the slab.

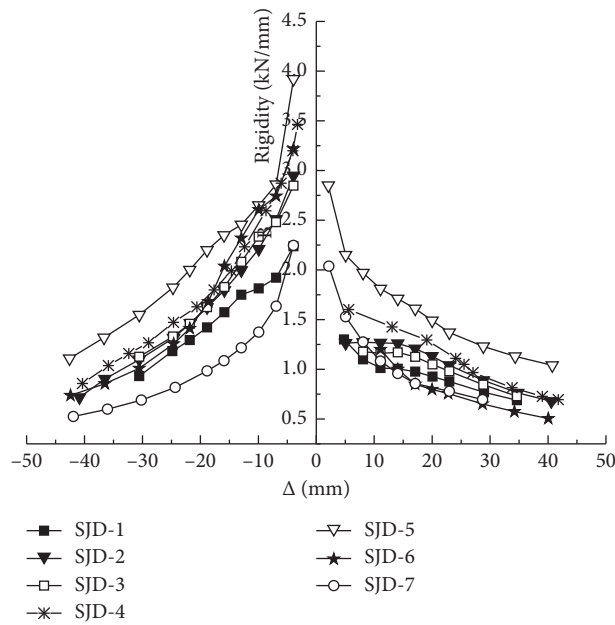


FIGURE 7: Curves of the rigidity degradation.

performance. From analysis, these errors exist despite the weld seams at the joints, the bond slip between the steel tube and the concrete, and assumptions of idealised constitutive relationship and boundary conditions.

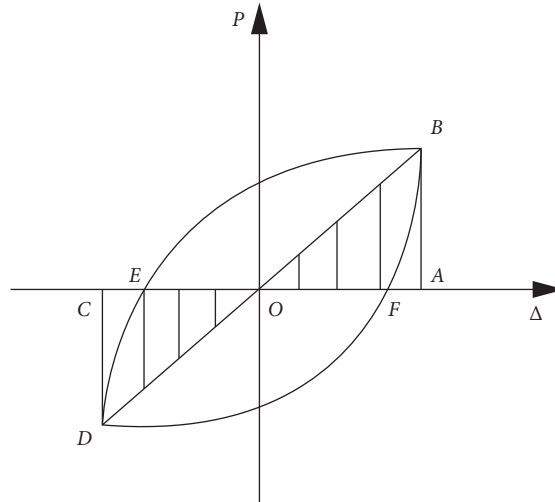
**5.4.2. Skeleton Curves.** As shown in Figure 14, the skeleton curves obtained from the physical tests and FEM simulation are in good agreement with each other. The skeleton curves are S-shaped, which indicates that the specimens have undergone elastic, elastic-plastic, and plastic stages consecutively.

In addition, induced by the composite effect of the slab and the steel beam, the skeleton curves are asymmetrically distributed, and the bearing capacity and rigidity in the positive direction are larger than those in the negative direction. The symmetry of the skeleton curves obtained from the FEM analysis is better than that from the physical tests. This symmetry is induced by no consideration of the residual deformation of the members, avoiding the torsion of members by imposing a constraint in the FEM analysis. In the test, the residual deformation and torsion of members are inevitable.

TABLE 4: Key points and ductility index.

Specimen	Force direction	Yield load $P_y$ (kN)	Yield displacement $\Delta_y$ (mm)	Peak load $P_u$ (kN)	Peak displacement $\Delta_u$ (mm)	Ductility index $\mu$	Average value $\mu$
SJD-1	+	17.1	16.8	23.9	34.6	2.06	1.90
	-	-26.5	-17.5	-31.3	-30.6	1.75	
SJD-2	+	19.4	15.8	27.6	40.6	2.57	2.47
	-	-28.3	-15.4	-34.9	-36.5	2.37	
SJD-3	+	18.5	17.1	25.7	34.6	2.03	2.03
	-	-28.5	-15.0	-35.0	-30.6	2.04	
SJD-4	+	19.6	14.8	27.1	35.6	2.41	2.31
	-	-28.0	-16.4	-34.9	-36.5	2.22	
SJD-5	+	31.0	15.0	43.6	28.7	1.91	1.98
	-	-39.0	-17.8	-49.8	-36.5	2.05	
SJD-6	+	13.4	16.1	20.3	39.0	2.42	1.90
	-	-30.8	-13.3	-33.5	-18.0	1.36	
SJD-7	+	18.2	22.8	21.1	39.0	1.72	2.10
	-	-15.8	-16.4	-22.2	-40.9	2.49	

Note. "+" denotes positive direction, and "-" denotes the negative direction.

FIGURE 8: Idealised  $P$ - $\Delta$  hysteretic loop.

5.4.3. *Comparison of Typical Specimen Failure Modes.* Figures 15–18 show that the failure modes observed in the tests and the simulation are in agreement with each other. Because the weld seams were not considered, the failure of specimens in FEM occurs at locations with the largest deformation. From observation, the local buckling and rupture failures generally occur at the connections where the H-shaped steel beam is linked to the steel ring-stiffener.

5.4.4. *Stress Analyses of Joints.* As shown in Table 1, SJD-2 has a steel beam of dimensions  $150 \text{ mm} \times 75 \text{ mm} \times 5 \text{ mm} \times 5.5 \text{ mm}$ , while SJD-5 has a steel beam of  $200 \text{ mm} \times 100 \text{ mm} \times 5.5 \text{ mm} \times 6 \text{ mm}$ . The other parameters of the two joints are the same. A comparison of the parameters of SJD-2 and SJD-4 reveals that SJD-4 has high-strength bolts settled at the joint's core area,

while SJD-2 does not. The stress distributions of joints SJD-2, SJD-4, and SJD-5 are illustrated in Figures 19–21, respectively.

From Figure 19 (SJD-2), as the displacement of the beam-end far from the joint reaches 12 mm, the maximum normal stress, 375.4 MPa, occurs at the trapezoidal zone of both the steel beam flanges. The normal stress at the trapezoid zone increases with displacement, and reaches 451 MPa at 18 mm. After 18 mm, the normal stress gradually yields. At 30 mm, the normal stress near the bolt-weld connection partially yields and local buckling occurs at both the flanges. At 36 mm, the lower flange of the steel beam near the bolt-weld connection yields significantly. Although the top flange of the steel beam near the bolt-weld connection has yielded, the deformation is negligible for the supporting and constraint effects of the slab. At 39 mm, the local buckling area of the lower flange near the bolt-weld connection has significantly enlarged, and hence completely failed.

TABLE 5: Energy dissipation parameters.

Displacement (mm)	SJD-1		SJD-2		SJD-3		SJD-4		SJD-5		SJD-6		SJD-7	
	$E$	$h_e$												
3	0.137	0.022	0.069	0.011	0.078	0.012	0.088	0.014	0.201	0.032	0.064	0.01	0.074	0.012
6	0.114	0.018	0.151	0.024	0.096	0.015	0.214	0.034	0.154	0.025	0.084	0.013	0.095	0.015
9	0.126	0.02	0.223	0.036	0.112	0.018	0.292	0.047	0.2	0.032	0.128	0.02	0.12	0.019
12	0.155	0.025	0.259	0.041	0.239	0.038	0.365	0.058	0.226	0.036	0.213	0.034	0.147	0.023
15	0.289	0.046	0.318	0.051	0.338	0.054	0.399	0.064	0.236	0.038	0.296	0.047	0.197	0.031
18	0.352	0.056	0.358	0.057	0.395	0.063	0.453	0.072	0.322	0.051	0.409	0.065	0.248	0.039
21	0.441	0.07	0.466	0.074	0.499	0.079	0.523	0.083	0.44	0.07	0.411	0.065	0.415	0.066
24	0.549	0.087	0.591	0.094	0.878	0.14	0.591	0.094	0.57	0.091	0.52	0.083	0.54	0.086
30	1.045	0.166	0.883	0.141	0.867	0.138	0.892	0.142	0.879	0.14	0.834	0.133	0.792	0.126
36	1.244	0.198	1.201	0.191	1.181	0.188	1.206	0.192	1.049	0.167	1.03	0.164	1.012	0.161

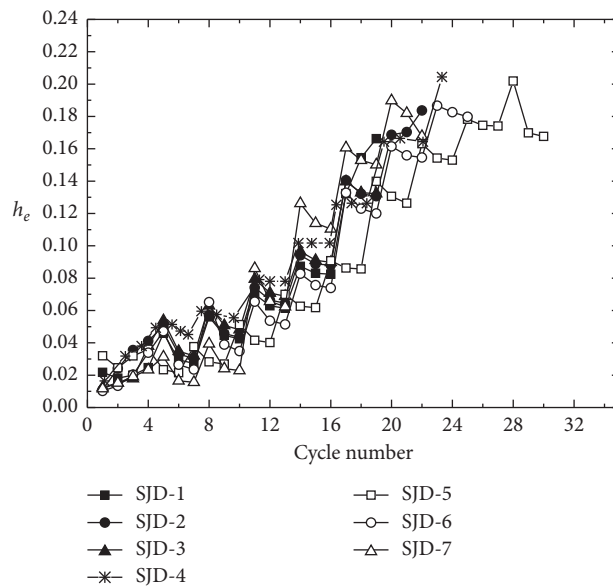


FIGURE 9: Curves of equivalent viscous damping coefficient vs. cycle number.

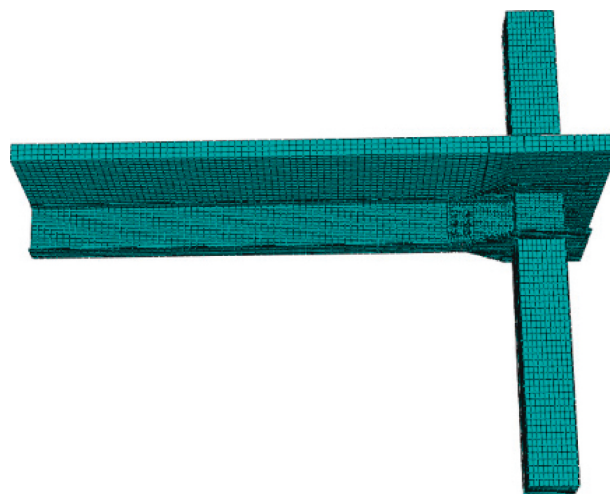


FIGURE 10: Meshing.

From Figure 20 (SJD-4), the maximum normal stress, 349.1 MPa, occurs near the bolt-weld connection at a displacement of 12 mm for the strengthening effect of the bolts.

At 18 mm, the normal stress at the flanges near the bolt-weld connection increases significantly and reaches 451.77 MPa. It follows that the high-strength bolts located at the joint's

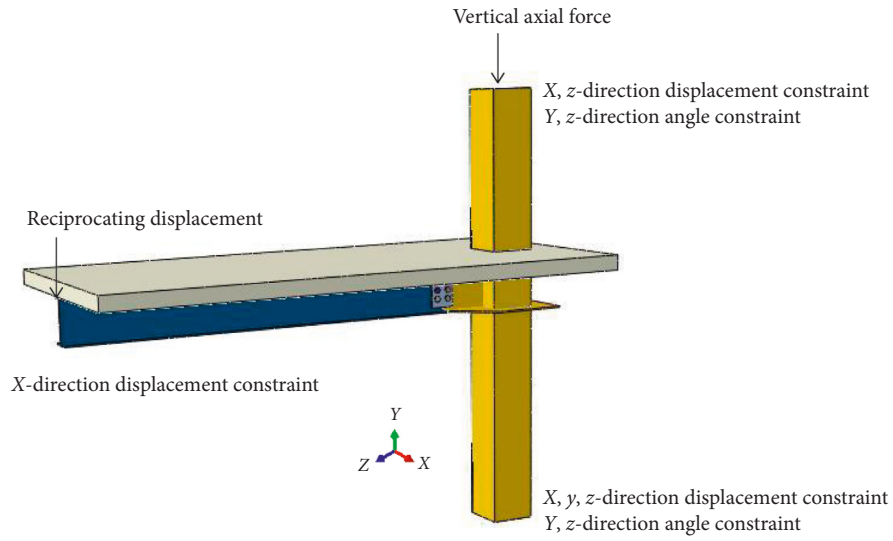


FIGURE 11: Loading and boundary conditions.

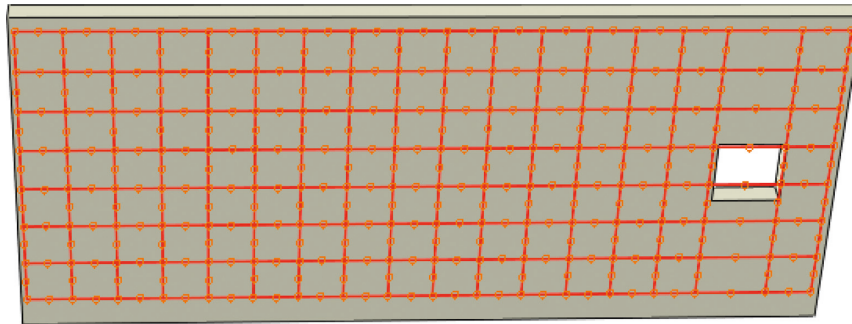


FIGURE 12: Modelling of reinforcing bars and recycled concrete slab.

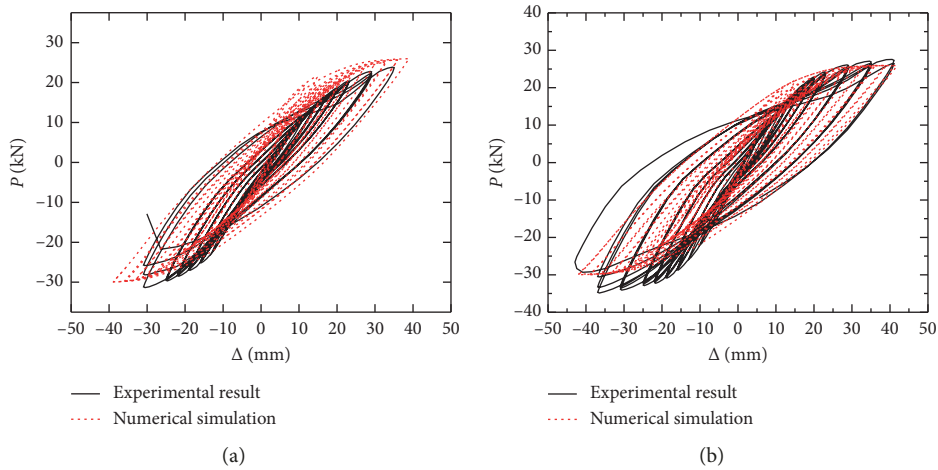


FIGURE 13: Continued.

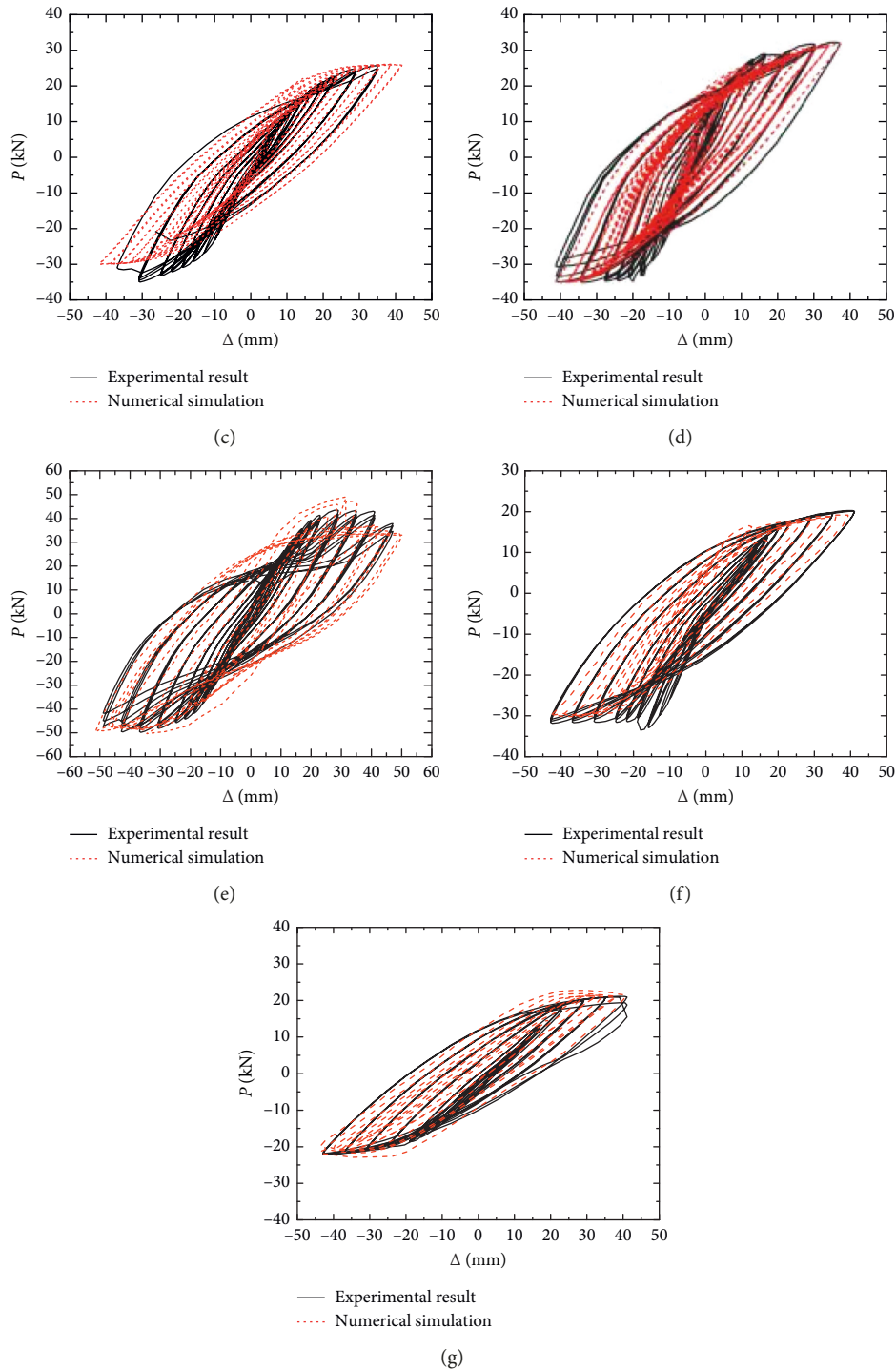
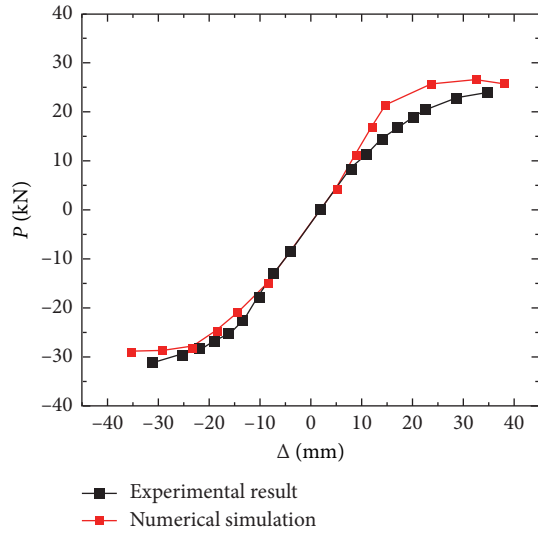


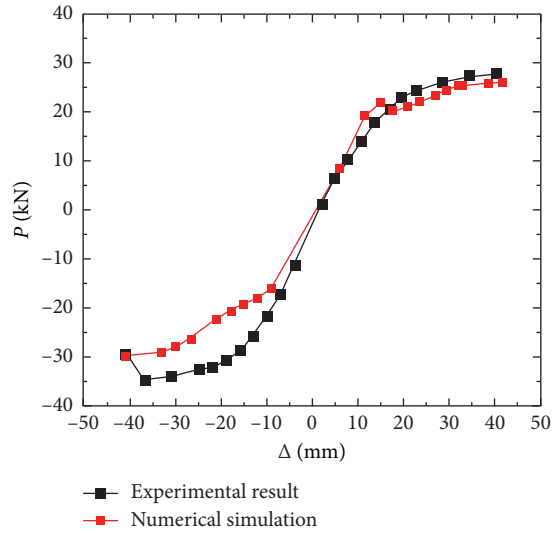
FIGURE 13: Comparison of hysteretic curves. (a) SJD-1. (b) SJD-2. (c) SJD-3. (d) SJD-4. (e) SJD-5. (f) SJD-6. (g) SJD-7.

core area not only protect the core area from failure, but also changes the distribution of stresses. At 30 mm, the normal stress at the flanges near the bolt-weld connection increases to a value smaller than that of SJD-2. At the moment, both the flanges have partially yielded. At 36 mm, the yielding areas of the two flanges enlarge, and a larger local buckling is observed. At 42 mm, the local buckling area near the bolt-weld connection enlarges significantly, and the flanges enter the plastic stage.

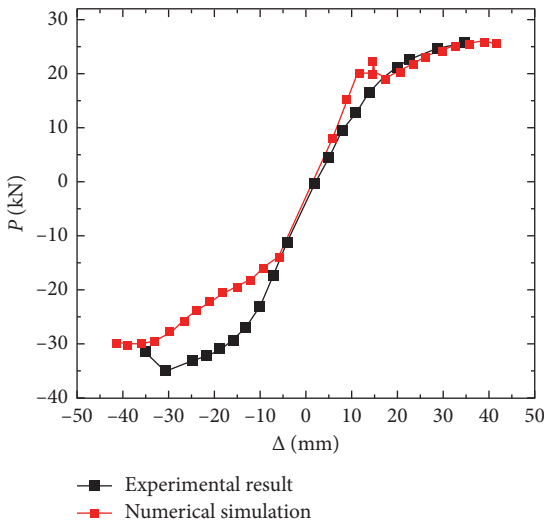
From Figure 21 (SJD-5), the maximum normal stress, 332.17 MPa, which is 43.23 MPa less than in SJD-2, occurs near the bolt-weld connection at a displacement of 12 mm. It follows that the increased cross section of the steel beam can decrease the stresses in the ring-stiffener, thus protecting the joint's core area. At 18 mm, the normal stress at the flanges near the bolt-weld connection increases significantly, and reaches 423.35 MPa. At 24 mm, the normal stress near the connection starts to yield. At 30 mm, the yielded area of both



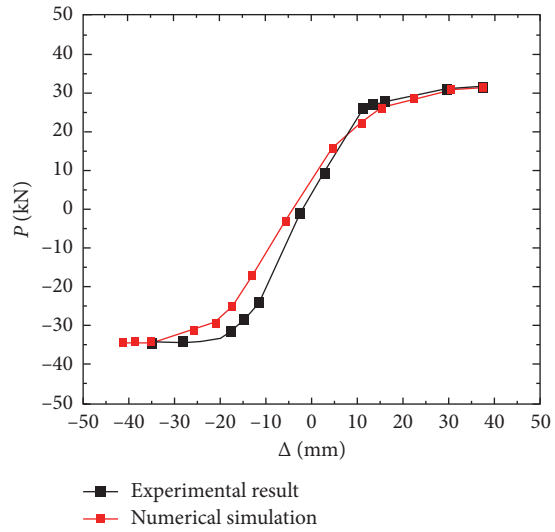
(a)



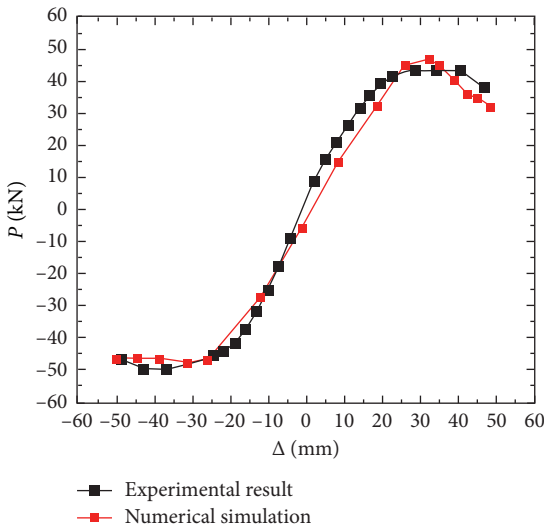
(b)



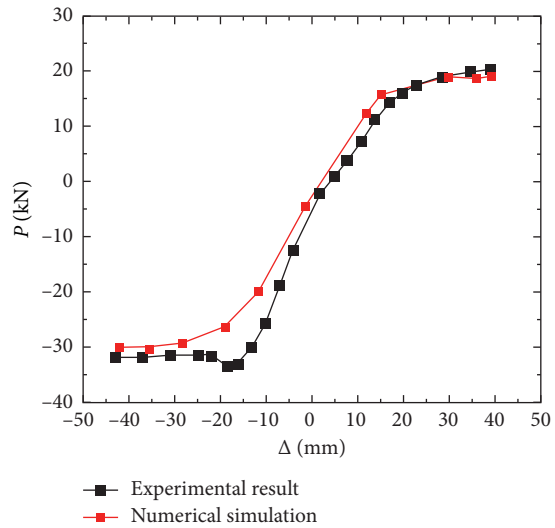
(c)



(d)



(e)



(f)

FIGURE 14: Continued.

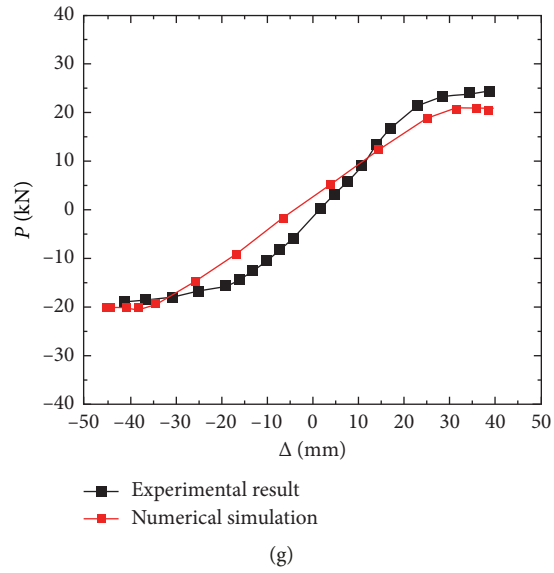


FIGURE 14: Comparison of the skeleton curves. (a) SJD-1. (b) SJD-2. (c) SJD-3. (d) SJD-4. (e) SJD-5. (f) SJD-6. (g) SJD-7.

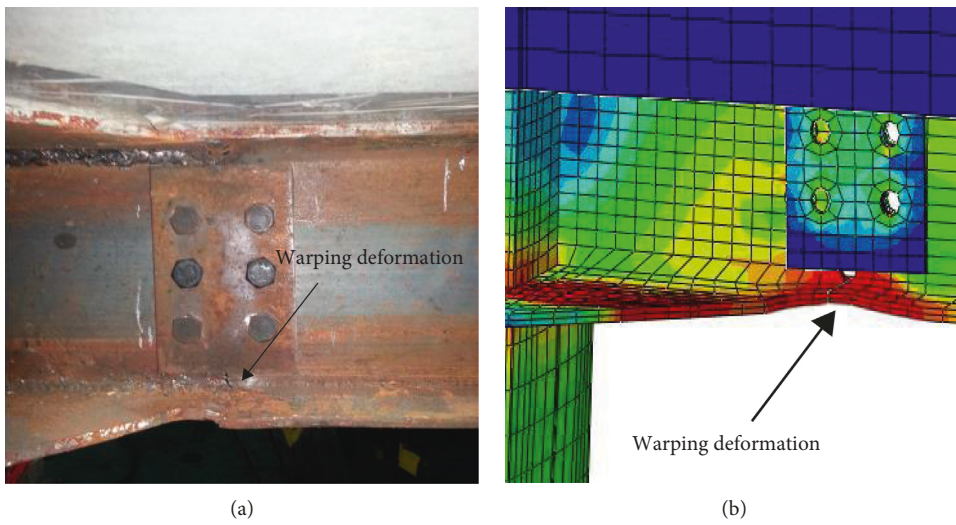


FIGURE 15: Damage comparison of SJD-1.

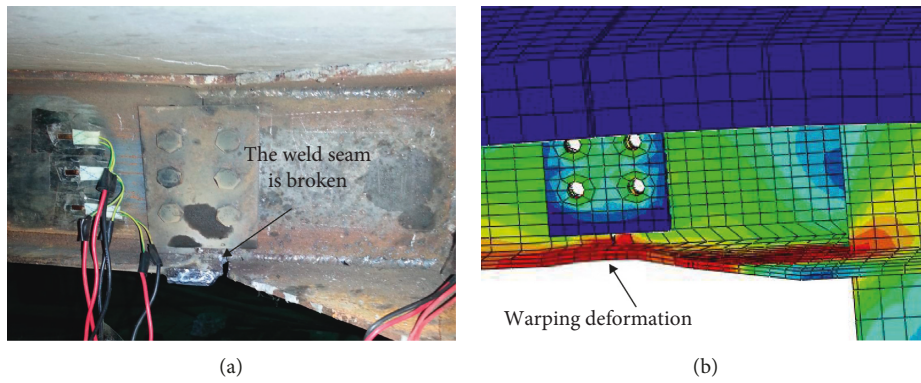


FIGURE 16: Damage comparison of SJD-2.

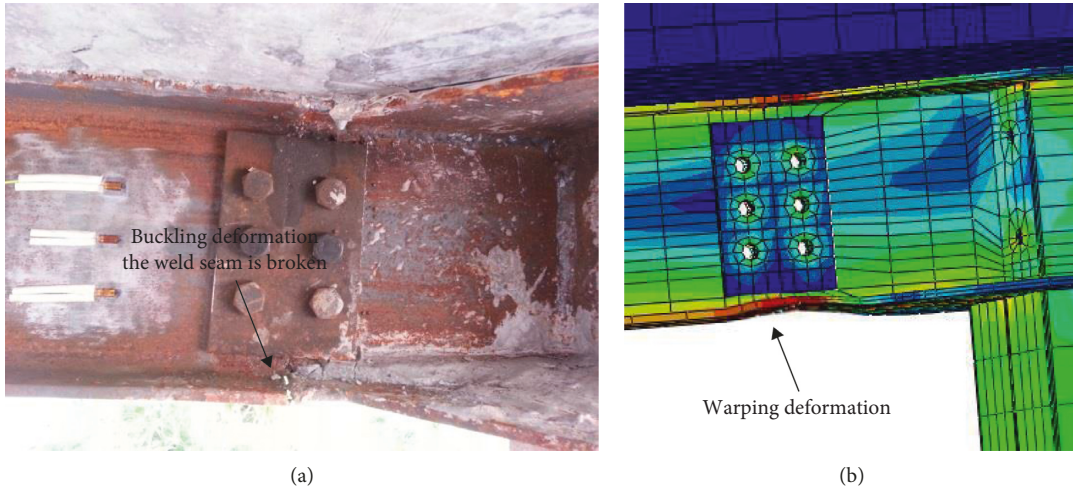


FIGURE 17: Damage comparison of SJD-2.

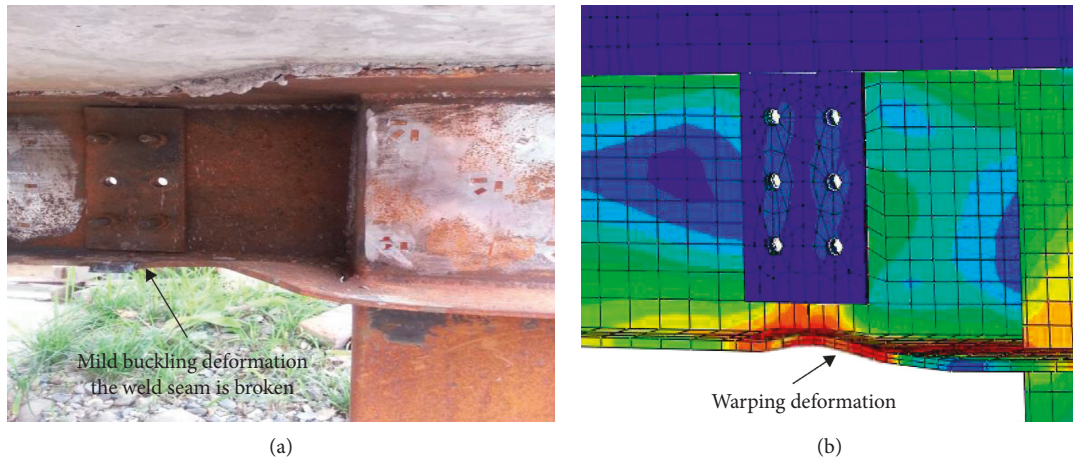


FIGURE 18: Damage comparison of SJD-5.

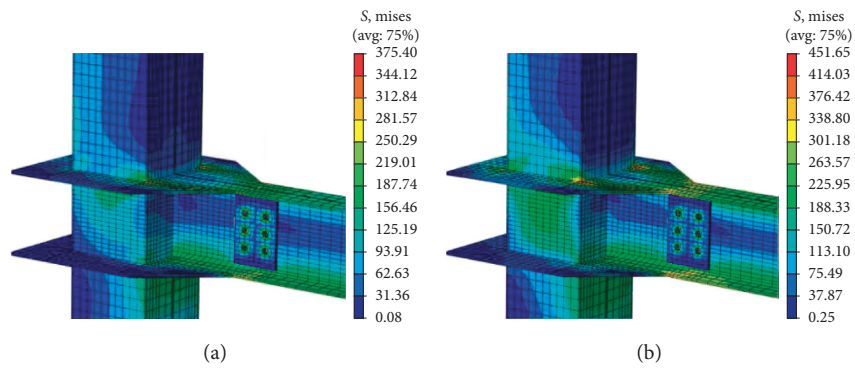


FIGURE 19: Continued.

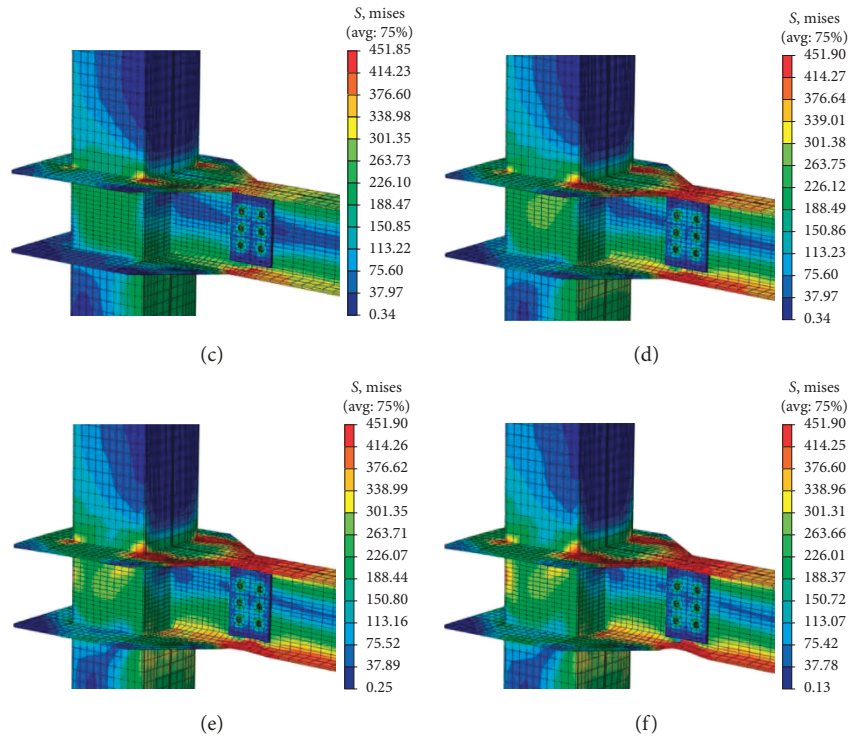


FIGURE 19: Stress distribution of SJD-2 at various displacements (in mm). (a) 12 mm. (b) 18 mm. (c) 24 mm. (d) 30 mm. (e) 36 mm. (f) 39 mm.

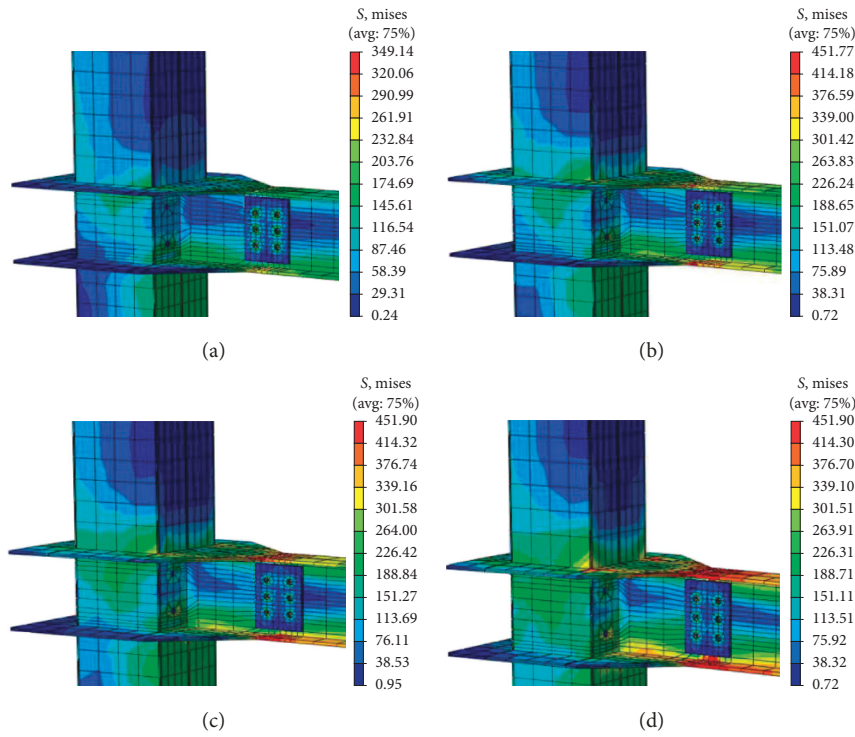


FIGURE 20: Continued.

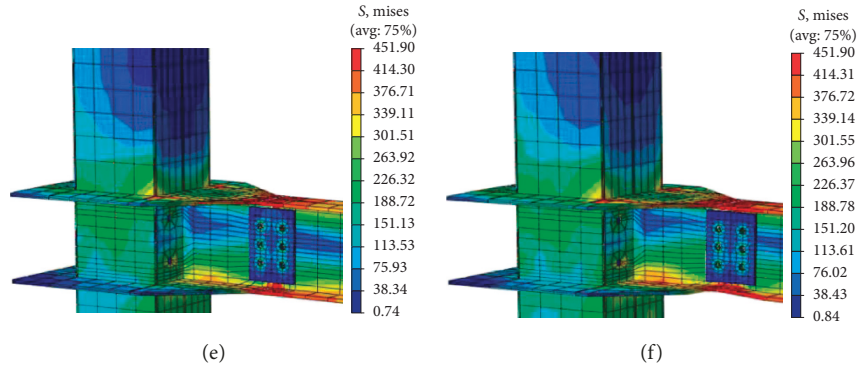


FIGURE 20: Stress distribution of SJD-4 at various displacements (in mm). (a) 12 mm. (b) 18 mm. (c) 24 mm. (d) 30 mm. (e) 36 mm. (f) 42 mm.

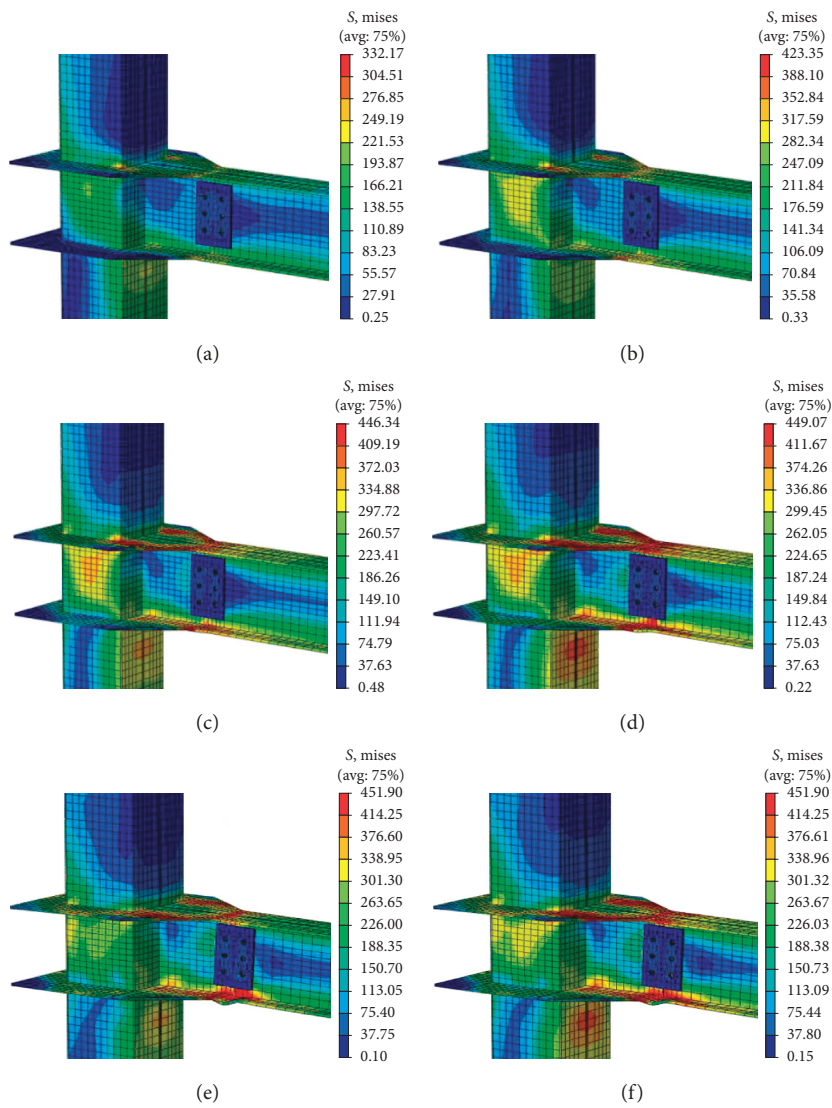


FIGURE 21: Stress distribution of SJD-5 at various displacements (in mm). (a) 12 mm. (b) 18 mm. (c) 24 mm. (d) 30 mm. (e) 36 mm. (f) 39 mm.

flanges near the connection enlarges. At 39 mm, the normal stress near the connection enlarges significantly, along with the plastic region. At the moment, the upper flange

undergoes an insignificant deformation with the constraint of the slab; the lower flange undergoes significant local buckling and has now completely yielded.

## 6. Conclusions

In this study, the seismic performance of ESRS joints was studied via physical tests and FEM simulation. The following is a summary of the main conclusions of the study:

- (1) After the elastic, elastic-plastic, and failure stages, a plastic hinge begins to form gradually at the beam-end near the joint. For minor displacements and strains, the column and joint are elastic. Therefore, the designed specimens of joints meet the seismic principles of strong column and weak beam, and strong joint and weak member.
- (2) As the ESRS can effectively transmit and distribute the load, the distribution of stresses within the joint's core area is more uniform. This contributes to the seismic performance of joints. Due to the composite effects of slabs, the joints' rigidity, bearing capacity, and energy dissipation capacity, and the local stability of the steel beam's top flange and the integral stability of the steel beam are enhanced. The rigidity and bearing capacity of joints in the negative direction are larger than that in the positive direction.
- (3) The bearing capacity, strength degradation, ductility, and energy dissipation of the specimens were barely influenced by the axial compressive ratio. Instead, the bearing capacity and rigidity were significantly influenced by the beam-column linear stiffness ratio, and increased with an increase in the ratio. The ductility and energy dissipation capacity of specimens, however, decreased with the ratio. Since the plastic hinge occurred at the beam-end but not in the joint's core area, the bearing capacity, rigidity, and energy dissipation capacity of specimens were not influenced by the high-strength bolts fastened in the joint's core area. Subjected to the same axial compressive ratio, the ductility and energy dissipation capacity of specimens with recycled concrete slab were higher than those of the specimens with the slab-profiled-steel-sheet composite.
- (4) Compared with the existing reinforced concrete joints, the ESRS joints developed in this paper not only have the advantages of higher ductility, larger effective viscous damping factor, better energy dissipation capacity, and plumper hysteretic curves without pinching, but also simple construction and definite load-transferring mechanism. We believe that the technique will benefit structural and civil engineers in developing better earthquake-resistant buildings, and the recycled concrete will benefit the environment and reduce costs.
- (5) Large-scale finite element software ABAQUS was used to simulate the seismic performance of the ESRS joints. A joint stress analysis was performed to ensure the correctness of the model. From observation and simulation, the normal stresses in the ring stiffener were generally uniform, increased from the

longer side to the opposite shorter side of the trapezoidal zone, and reached the maximum value near the bolt-weld connection. To avoid damage to the ring-stiffener during engineering practice, we can thicken it or add rib-strengthened panels.

## Data Availability

All the data used in this study are available from the experimental tests of the composite joints, and data can be obtained from the corresponding author upon reasonable request.

## Conflicts of Interest

The author(s) declare(s) that there are no conflicts of interest regarding the publication of this paper.

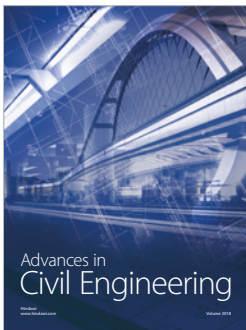
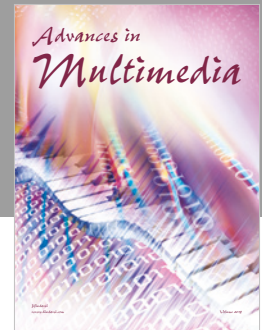
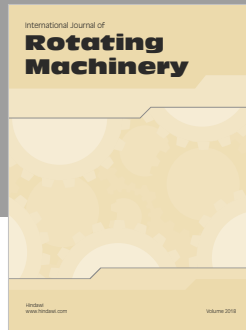
## Acknowledgments

This study was financially supported by the National Natural Science Foundation of China (NSFC) (Grant no. 51308479), the Department of Education Funded Project of Sichuan, China (Grant no. 18CZ0012), the Science and Technology Research Projects of Mianyang, China (Grant no. 15S-02-3), the Shock and Vibration of Engineering Materials and Structures Key Laboratory of Sichuan Province, China (Grant no. 18kfgk14), the Applied Basic Research Project of Sichuan Science and Technology Department (Grant no. 2018JY0443), and the Doctoral Foundation Project of Southwest University of Science and Technology (Grant no. 19zx7110).

## References

- [1] L.-H. Han, *Concrete Filled Steel Tube Structure*, Science Press, Beijing, China, 2004, in Chinese.
- [2] N. Li, J.-H. Zhao, J. Wang, and J. Yin, "Numerical analysis of steel fiber reinforced high strength concrete filled steel tubular short columns under axial compression load," *Concrete*, vol. 1, pp. 20–24, 2016.
- [3] J. Yin, "Research on the axial compression property of steel fiber reinforced lightweight aggregate concrete filled steel tubes after exposure to fire," Masteral Dissertation, Ningbo University, Ningbo, China, 2012.
- [4] S. R. Gopal and P. D. Manoharan, "Tests on fiber reinforced concrete filled steel tubular columns," *Steel and Composite Structures*, vol. 4, no. 1, pp. 37–48, 2004.
- [5] W.-H. Jin, Z.-X. Liu, S.-Y. Liu et al., "Experimental study of ultra-high performance fiber reinforced concrete filled steel tube columns under blast loading," *Building Structure*, vol. 46, no. 4, pp. 45–49, 2016.
- [6] Y.-Y. Lu, J. Chen, and S. Li, "Experimental research on steel fiber reinforced high strength concrete filled steel tubular short columns subjected to axial compression load," *Journal of Building Structures*, vol. 32, no. 10, pp. 166–172, 2011.
- [7] Q.-J. Ding, R.-J. Liu, T.-M. Mou, and X. Song, "Investigation on toughness of steel fibre reinforced self-compacting micro-expansion concrete-filled steel tube," *Journal of Southeast University*, vol. 40, pp. 10–14, 2010.

- [8] S. Tokgoz and C. Dunder, "Experimental study on steel tubular columns in-filled with plain," *Steel Construction*, vol. 7, p. 88, 2010.
- [9] J. Chen, Y.-Y. Lu, and S. Li, "Theoretical Analysis of Steel Fiber Reinforced high strength concrete filled steel tube under axial compression," *Engineering Mechanics*, vol. 28, no. 9, pp. 115–121, 2011.
- [10] S. Tokgoz and C. Dunder, "Experimental study on steel tubular columns in-filled with plain and steel fibre reinforced concrete," *Thin-Walled Structures*, vol. 48, no. 6, pp. 414–422, 2010.
- [11] G. Campione, L. L. Mendola, L. Sanpaolesi, N. Scibilia, and G. Zingone, "Behavior of fiber reinforced concrete-filled tubular columns in compression," *Materials And Structures*, vol. 35, no. 6, pp. 332–337, 2002.
- [12] S. R. Gopal and P. D. Manoharan, "Experimental behaviour of eccentrically loaded slender circular hollow steel columns in-filled with fibre reinforced concrete," *Journal of Constructional Steel Research*, vol. 62, no. 5, pp. 513–520, 2006.
- [13] G. B. /T228.1-2010, *Metal Material Tensile test (Part 1: Test Method for room Temperature)*, China Planning Press, Beijing, China, 2010, in Chinese.
- [14] Z.-Q. Zhang, J.-H. Zhao, and Y. Xu, "Experimental research on axial compression behavior of steel fiber reinforced recycled aggregate concrete-filled circular steel tubular short columns," *Concrete*, no. 1, pp. 5–8, 2016.
- [15] Z.-Q. Zhang, J.-H. Zhao, and Y.-J. Deng, "Experimental research on axial compression behavior of steel fiber reinforced recycled aggregate concrete-filled square steel tubular short columns," *Industrial Construction*, vol. 48, no. 11, pp. 168–174, 2018.
- [16] H.-Y. Dong, R.-J. Li, W.-L. Cao, and Q. Qiao, "Axial compression performance of rectangular concrete-filled steel tubular columns with different cell details," *Journal of Building Structures*, vol. 37, no. 5, pp. 69–81, 2016.
- [17] X.-X. Zha, Y.-T. Li, and S.-T. Zhong, "Unified formula for axial compression combined strength of circular, polygonal, solid and hollow CFST columns," in *Proceedings of the National Steel Structure Academic Annual Conference*, pp. 177–181, China Steel Structure Society, Beijing, China, August 2010.
- [18] X.-W. Li, J.-H. Zhao, T.-D. Zhu, and L. Wang, "Mechanics behavior of axially loaded short columns with concrete-filled square steel tube," *China Journal of Highway And Transport*, vol. 19, no. 4, pp. 77–81, 2006.
- [19] JGJ/T101-2015, *Specification for Seismic Test of Building*, China Building Industry Press, Beijing, China, 2015, in Chinese.
- [20] J.-R. Tang, *Seismic Strengthening of Reinforced Concrete Frame Joints*, Southeast University Press, Nanjing, China, 1989, in Chinese.
- [21] L.-H. Han, Z. Tao, and W.-D. Wang, *Modern Combined Structures and Hybrid Structures—Experiments, Theories and Methods*, Science Press, Beijing, China, 2009, in Chinese.
- [22] A. R. Tamboli, *Steel Design Handbook: LRFD Method*, McGraw-Hill, New York, NY, USA, 1997.
- [23] H.-F. Chen, L.-P. Sa, and T.-Q. Yu, *Elasticity and Plasticity*, China Building Industry Press, Beijing, China, 2004.
- [24] J.-Z. Xiao, *Recycled Concrete*, China Building Industry Press, Beijing, China, 2008.
- [25] GB50010-2010, *National Standards of People's Republic of China. Code for Design of Concrete Structures*, China Building Industry Press, Beijing, China, 2010, in Chinese.
- [26] Y.-F. Yang, "Theoretical research on load-deformation relation of recycle aggregate concrete-filled steel tubular members," *Industrial Construction*, vol. 37, no. 12, pp. 1–6, 2007.
- [27] E.-C. Meng, "Study on seismic behavior of hybrid frame structure with RAC filled deep flexural beam," Doctoral Dissertation, Guangxi University, Nanning, China, 2016.
- [28] V. Birtel and P. Mark, "Parameterised finite element modelling of RC beam shear failure," in *Proceedings of the ABAQUS Users' Conference*, Boston, MA, USA, May 2006.



**Hindawi**

Submit your manuscripts at  
[www.hindawi.com](http://www.hindawi.com)

